Research Square

Preprints are preliminary reports that have not undergone peer review.
They should not be considered conclusive, used to inform clinical practice,
or referenced by the media as validated information.

Polarization-Controlled MHz Burst-Mode Femtosecond Laser Slicing of n-Type 4H-SiC Wafers

Kai-Chieh Hsu
National Yang Ming Chiao Tung University
Jia-Fan Kuo
National Yang Ming Chiao Tung University
Chung-Wei Cheng
weicheng@nycu.edu.tw

National Yang Ming Chiao Tung University https://orcid.org/0000-0002-9994-0670

Research Article

Keywords: 4H-SiC, femtosecond laser, linear polarization, MHz burst mode, wafer slicing, crack connectivity

Posted Date: November 19th, 2026

DOI: https://doi.org/10.21203/rs.3.rs-11560860/v1

License: This work is licensed under a Creative Commons Attribution 4.0 International License.
Read Full License

Polarization-Controlled MHz Burst-Mode Femtosecond Laser Slicing of n-Type 4H-SiC Wafers

Kai-Chieh Hsu[1] Jia-Fan Kuo[1], and Chung-Wei Cheng[1,2*]

[1]*Department of Mechanical Engineering, National Yang Ming Chiao Tung University, No. 1001, Ta Hsueh Road, Hsinchu 300, Taiwan*

[2]*Heterogeneously-integrated Silicon Photonic Integration Center, National Taiwan University of Science and Technology, No. 43, Section 4, Keelung Road, Taipei 106, Taiwan*

[*] Email: weicheng@nycu.edu.tw

Abstract

This study demonstrates that linear polarization can tune the balance between separation load and surface height variation in MHz burst-mode femtosecond laser slicing of 4° off-axis n-type 4H-SiC. Four polarization angles were compared using dual-pulse bursts with an intraburst repetition rate of approximately 18 MHz under fixed incident-face, scanning, and burst conditions. Optical microscopy and scanning electron microscopy were used to characterize internal modification, local lateral crack extension, and crack paths spanning adjacent scan lines. Tensile separation tests and laser scanning confocal microscopy were performed to measure nominal separation stress and separated-surface topography, respectively. By distinguishing local crack extension from multi-line crack morphology, these findings show that local crack length alone does not explain separation behavior and suggest contributions from crack-path continuity and residual connections.

Keywords: 4H-SiC, femtosecond laser, linear polarization, MHz burst mode, wafer slicing, crack connectivity

1. Introduction

The high hardness and brittleness of 4H-SiC make conventional mechanical slicing difficult, resulting in material loss, limited processing efficiency, and surface damage [1, 2]. Laser slicing provides an alternative by focusing energy inside the crystal to form modified regions and microcracks. Subsequent crack extension and interconnection enable wafer separation [3].

Crystal orientation and off-axis geometry affect crack propagation in n-type 4H-SiC. For a wafer with a nominal off-axis angle of 4°, the basal planes are inclined relative to the wafer surface. Cracks associated with cleavage planes can therefore extend at different heights and form stepped separation surfaces. Yamada et al. [3] showed that the scanning direction affects cleavage extension and interconnection in off-axis SiC. Li et al. [4] investigated the scanning direction relative to the step geometry and found changes in crack periodicity, exfoliation load, and surface roughness. This presents a practical challenge for laser slicing: the internally cracked layer should facilitate separation while limiting the height variation of the resulting surfaces. Processing conditions that reduce the separation load may therefore involve a trade-off in separated-surface topography. Yao et al. [5] compared n-type and semi-insulating (SI) 4H-SiC and further showed that the incident face and scanning orientation affect internal modification, crack extension, and separation behavior.

The morphology and connectivity of internal cracks also affect slicing performance. Qing et al. [6] classified five crack morphologies, related their formation to the processing energy, and compared the resulting separation stress and surface roughness. Wang et al. [7, 8] showed that subsequent scanning changes the stress conditions near existing crack tips, while connections between cracks at different depths influence crack growth and the load required for separation. These findings indicate that local crack dimensions and connections between adjacent modified tracks should be examined separately when evaluating slicing behavior.

Temporal pulse delivery can be used to regulate internal modification. During femtosecond laser propagation in SiC, nonlinear effects, including pre-focal plasma shielding and self-focusing, can limit energy localization at the target depth. Yan et al. [9] used temporally shaped pulse trains with a sub-pulse spacing of approximately 0.47 ps to modify SI 4H-SiC. Adjusting the total pulse-train energy and the number of sub-pulses improved energy deposition near the focus and produced thin, single-layer modified and cracked regions. At a longer sub-pulse interval, Chen et al. [10] applied 18 MHz intraburst irradiation to n-type 4H-SiC. These results establish temporal pulse delivery as a means of adjusting slicing behavior. Whether polarization can further modify crack morphology and the balance between separation load and surface height variation under fixed burst conditions remains to be examined.

In addition to pulse timing, linear polarization affects the morphology of internal modification. Sun et al. [11] investigated picosecond laser slicing of SI 4H-SiC and showed that the polarization direction relative to the scanning direction changes the modified-track width, lateral cracking, and longitudinal damage. However, it remains unclear whether polarization-dependent local crack extension is sufficient to explain separation behavior in n-type 4H-SiC processed with dual-pulse MHz bursts. Local crack dimensions and crack paths spanning adjacent scan lines describe different aspects of the modified layer, and their relationships with separation load and surface height variation need to be distinguished.

In this study, linear polarization was varied while the incident face, crystal orientation, scanning direction, and burst parameters were fixed. Local lateral cracks and multi-line crack morphologies were examined, followed by measurements of separated-surface topography and nominal separation stress. The aim was to assess whether local crack length alone provides an adequate description of slicing behavior and to examine the additional insight offered by multi-line crack morphology.

2. Experimental Methods

2.1 Experimental setup

Figure 1(a) shows the femtosecond laser processing system. The laser source (FS-MM, mRadian) operated at a wavelength of 1030 nm with a pulse duration of 221 fs, an output beam diameter of 2 mm ($1/e^2$), and a maximum average power of 4.8 W. The burst repetition rate was adjustable from 100 to 1000 kHz. Within each burst, consecutive sub-pulses were separated by approximately 56 ns, corresponding to an intraburst repetition rate of approximately 18 MHz. A half-wave plate was used to adjust the linear polarization direction, and the beam was focused inside the specimen using a 50× objective lens (NA = 0.65). An Aerotech A3200 controller synchronized XY scanning, Z positioning, and laser emission. Before processing, the specimens were ultrasonically cleaned in ethanol for 10 min, mounted on a ceramic carrier using a thermal-release adhesive, and fixed to the processing stage by vacuum suction.

An n-type 4H-SiC wafer (Atecom) with a thickness of 350 ± 25 μm, an initial surface roughness $R_a \leq 0.5$ nm, and a nominal off-axis angle of 4° ± 0.5° was used. Figure 1(d) defines the off-axis angle between the surface normal and the crystal c-axis directed toward the C-face. Square specimens of approximately 5 × 5 mm² were prepared along the $[1\bar{1}00]$ and $[11\bar{2}0]$ directions. As shown in Figure 1(b), the laser was incident normally on the C-face, and the internal processing depth d was set to 200 μm. The scanning direction S was opposite to $[1\bar{1}00]$, and the area-filling direction was opposite to $[11\bar{2}0]$. The spacing between adjacent scan lines was defined as the hatch distance (HD).

Figure 1(c) defines the polarization angle θ, measured counterclockwise from the scanning direction S to the electric-field axis E. The conditions at θ = 0°, 45°, 90°, and 135° are denoted as E0, E45, E90, and E135, respectively. E0 and E90 correspond to polarization parallel and perpendicular to the scanning direction. Area processing was performed by successively translating the scan path at a fixed polarization. The burst repetition rate, number of sub-pulses,

sub-pulse energy, and scanning speed were fixed at 300 kHz, two, 4 μJ, and 20 mm/s, respectively, giving a burst energy of 8 μJ [10].

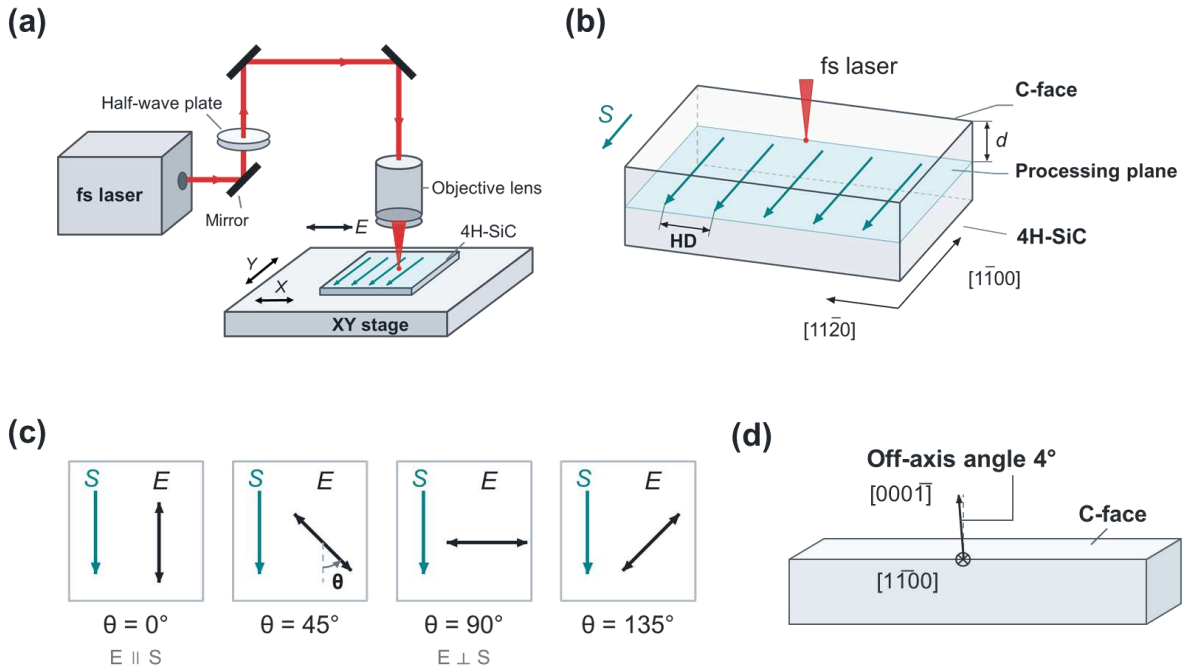


Figure 1 Schematic illustration of (a) femtosecond laser system, (b) internal scanning geometry, (c) polarization angle θ relative to the scanning direction S, and (d) 4° off-axis orientation of the 4H-SiC wafer

2.2 Separation tests and characterization

Figure 2(a1, a2) shows the specimen assembly for tensile separation. Both faces of each SiC specimen were bonded to 3D-printed polylactic acid (PLA) fixtures using a cyanoacrylate adhesive (Ergo 5210), with the loading axes aligned. The assembly was mounted in a universal testing machine (EZ Test, Shimadzu) with a maximum tensile load of 500 N. An axial load was applied at a crosshead speed of 500 mm/min to separate the specimen along the internally modified region. The loading configuration and separated specimen halves are shown in Figure 2(b) and (c), respectively. The nominal separation stress was calculated as $\sigma_{sep} = \frac{F_{max}}{A_{eff}}$, where

F_{max} is the maximum load during separation and A_{eff} is the initial specimen area obtained from the measured length and width. Three specimens were tested for each polarization condition.

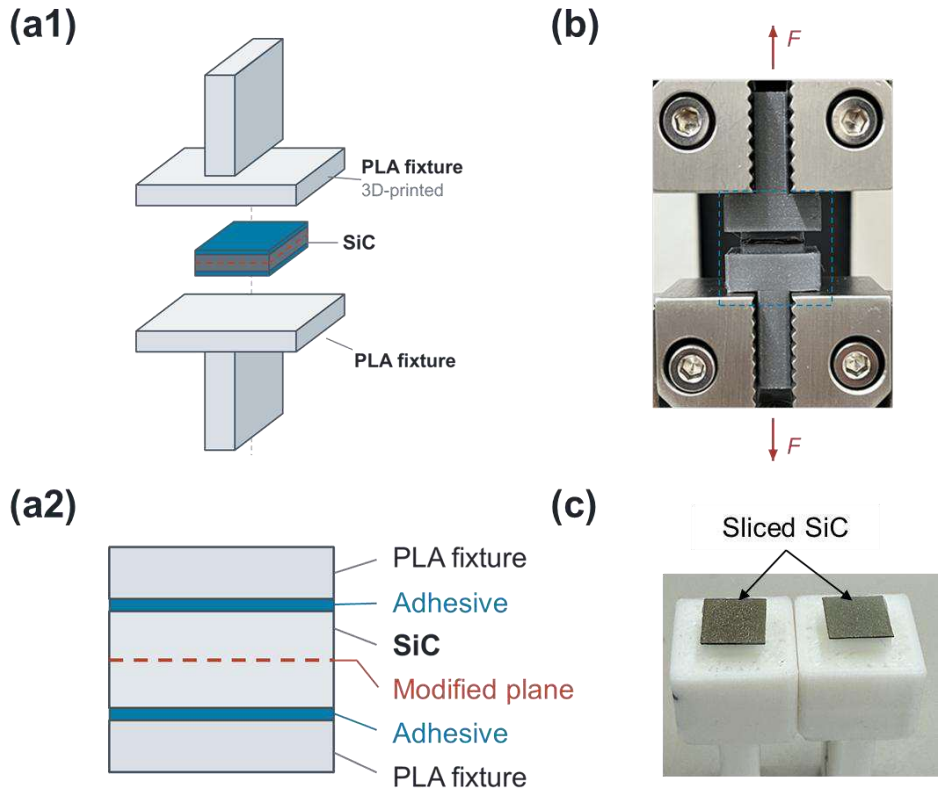


Figure 2 Tensile separation of laser-processed 4H-SiC: (a1) exploded view and (a2) cross-sectional schematic of the bonded specimen assembly, (b) tensile loading configuration, and (c) separated specimen halves

Top-view and cross-sectional morphologies were examined using optical microscopy (OM; VHX-7000N, Keyence). Scanning electron microscopy (SEM; SU-8010, Hitachi) was used to identify the modified-core boundaries, lateral crack tips, and local connections between adjacent processing positions. Top-view images were acquired through the incident surface to observe the internal processing region. Cross sections were perpendicular to the scan lines. After tensile separation, the lower exposed separation surface was used for separated-surface imaging.

The separated-surface topography was measured using a laser scanning confocal microscope (LSCM; VK-X3000, Keyence) with a full field of view of approximately 703 × 527 μm². Line profiles were extracted along the marked paths to compare inclined segments. The maximum surface height S_z was defined as the difference between the highest and lowest points within a selected rectangular region of approximately 500 × 500 μm². For each polarization condition, three measurements were summarized as the mean and sample standard deviation. Because an individual line profile and an areal measurement cover different sampling domains, the profile peak-to-valley range and S_z were evaluated separately.

3. Results and Discussion

3.1 Effect of polarization on internal modification morphology

Figure 3 presents the processing morphology at HD = 60 μm for polarization angles from 0° to 180° in 15° increments. The top-view OM images in Figure 3(a) show changes in the bright and dark regions between adjacent scan lines. Representative cross sections for E0, E45, E90, E135, and E180 are shown in Figure 3(b), where lateral modified regions are visible. Other elongated features on the prepared cross sections were attributed mainly to section preparation and fracture. E0 and E180 have equivalent linear-polarization axes and produce similar overall morphologies. In contrast, E45 and E135 differ in their local lateral features and in the morphology surrounding the modified regions. The results show that the internal morphology varies with polarization angle under the fixed incident-face and scanning conditions.

Sun et al. [11] reported polarization-dependent changes in modified-track width and lateral crack morphology in semi-insulator (SI) 4H-SiC. For n-type 4H-SiC, the arrangement of internal cracks also changes reflection and scattering, producing different intensity patterns in top-view observations [10]. The contrast variations in Figure 3 are therefore consistent with changes in both internal modification and crack geometry.

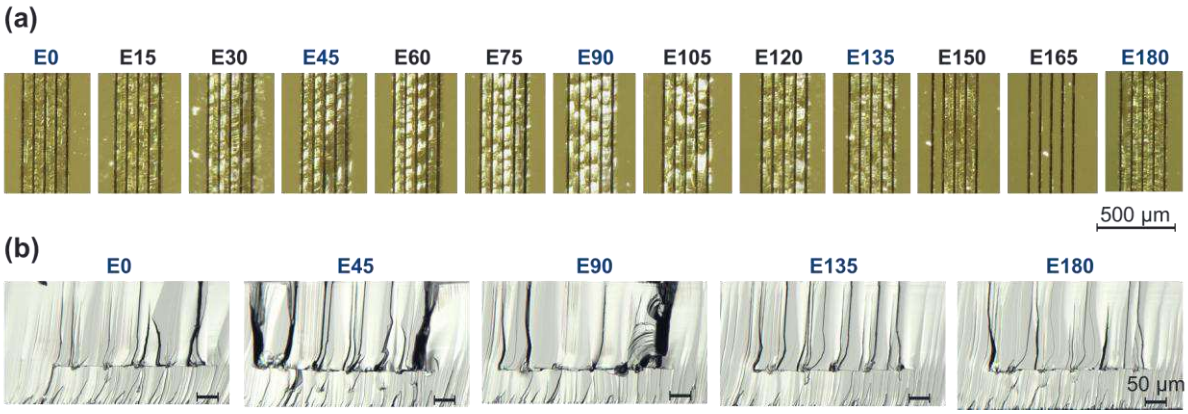


Figure 3 Effect of polarization angle on internal modification at HD = 60 μm: (a) top-view OM images from E0 to E180 in 15° increments and (b) cross-sectional OM images for E0, E45, E90, E135, and E180

To examine the local crack morphology, E0, E45, E90, and E135 were selected, and HD was increased to 70 μm. Figure 4(a1–d1) shows the cross-sectional OM images of the modified regions and their surroundings, while Figure 4(a2–d2) presents the corresponding local SEM images. Lateral cracks extend from both sides of the modified cores, with different visible crack-tip positions for the four polarization conditions.

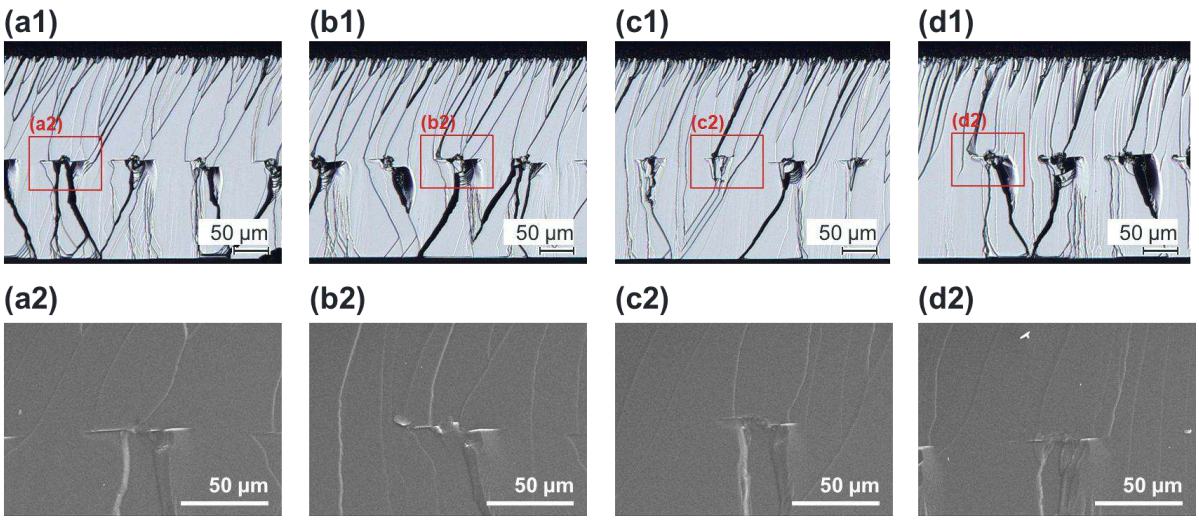


Figure 4 Effect of polarization on local crack morphology at HD = 70 μm: (a) E0, (b) E45, (c) E90, and (d) E135; (a1–d1) OM images and (a2–d2) corresponding SEM images of the regions marked by red boxes

Figure 5(a) defines the local lateral crack lengths. L_{left} and L_{right} are the projected distances from the left and right boundaries of the modified core to the corresponding visible crack tips, excluding the core width. Six pairs were used to calculate the mean crack length for each polarization condition. This quantity describes local lateral crack extension rather than the connectivity across multiple scan lines. As shown in Figure 5(b), the mean crack lengths are 22.9, 21.5, 15.5, and 16.9 μm for E0, E45, E90, and E135, respectively. The mean length decreases from E0 to E90 and then increases at E135.

Under the present conditions, E0 produces a greater mean local lateral crack length than E90. Sun et al. [11] reported the opposite trend for picosecond processing of SI 4H-SiC, with a greater crack-propagation width at E90 than at E0. Differences in material type and crack-size definitions should be considered when comparing the two studies. Nevertheless, both results indicate that linear polarization affects lateral cracking near the modified region.

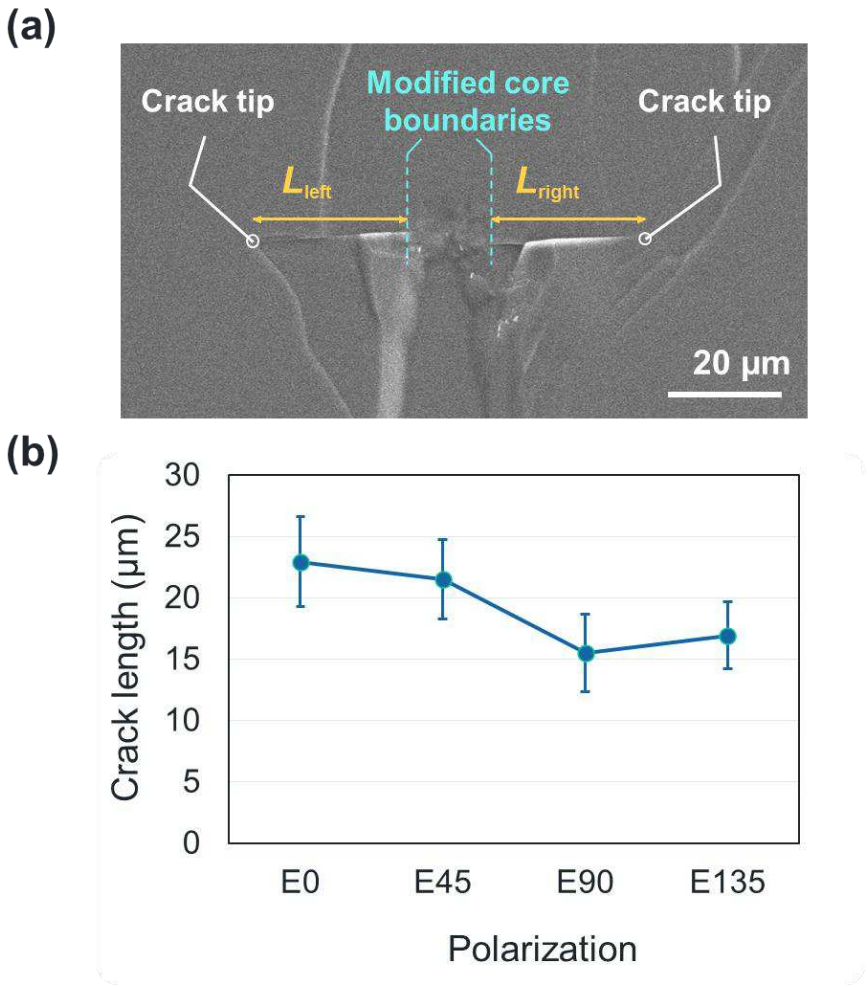


Figure 5 Effect of polarization on local lateral crack length at HD = 70 μm: (a) definition of L_{left} and L_{right} measured from the modified-core boundaries to the crack tips and (b) mean paired crack length for the four polarization conditions

Figure 6 shows representative SEM cross sections across multiple adjacent processing positions at HD = 60 μm. Lateral cracks are observed near the modified layer under all four polarization conditions, but their straightness, local height changes, and branching differ. E45 and E90 mainly show extended cracks, defined here as lateral cracks propagating obliquely across several modified lines. E0 and E135 mainly show local connections between cracks at neighboring positions.

During multi-line processing, the visible crack extent depends on interactions between neighboring tracks as well as the cracks formed near an individual modified core [6, 12]. Subsequent scans can change the stress conditions near existing crack tips and promote further extension. Cracks at different heights may also interact through local steps and fragmented junctions [7, 8, 13]. The morphologies in Figure 6 are consistent with these interactions, whereas the projected lengths in Figure 5 describe only the local crack extension.

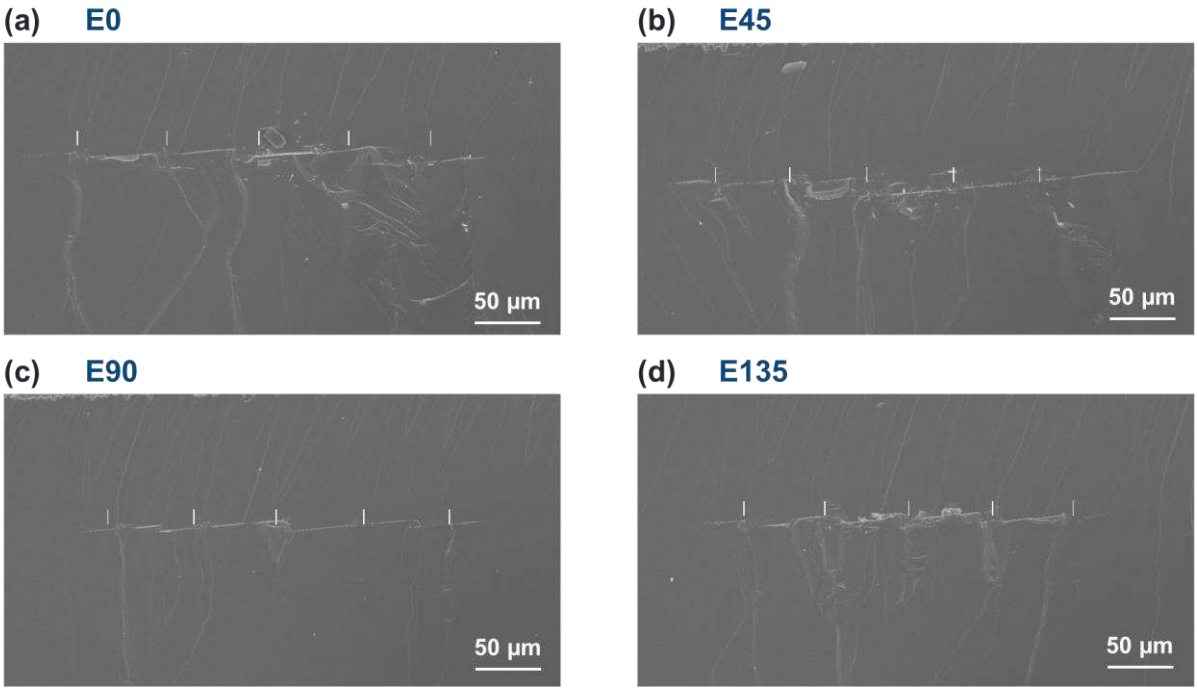


Figure 6 Effect of polarization on multi-line crack morphology at HD = 60 μm: cross-sectional SEM images for (a) E0, (b) E45, (c) E90, and (d) E135; white markers indicate the processing positions

3.2 Separated-surface morphology and height profiles

Figure 7 compares the top-view morphology of the internally modification region after laser processing with the morphology of the separated surface at HD = 60 μm. Directional textures are observed for all four polarization conditions, with differences in their characteristic scales and arrangements. E0 shows relatively fine, locally shell-like undulations. E45 produces

longer oblique stepped textures, whereas E90 shows more consistently aligned oblique features. E135 exhibits irregular local undulations and boundaries. The changes in the top-view and separated-surface patterns indicate that polarization affects both local modification and the larger-scale separation morphology.

The separated-surface textures can be interpreted as the combined imprints of modified tracks, inclined crack surfaces, and crack junctions. For 4° off-axis 4H-SiC, transitions between cleavage layers and incompletely connected regions can produce steps [4]. The scanning direction and crack-propagation geometry also affect surface height variation and texture alignment [5]. The differences in Figure 7 may therefore be associated with changes in the extension and intersection of crack surfaces.

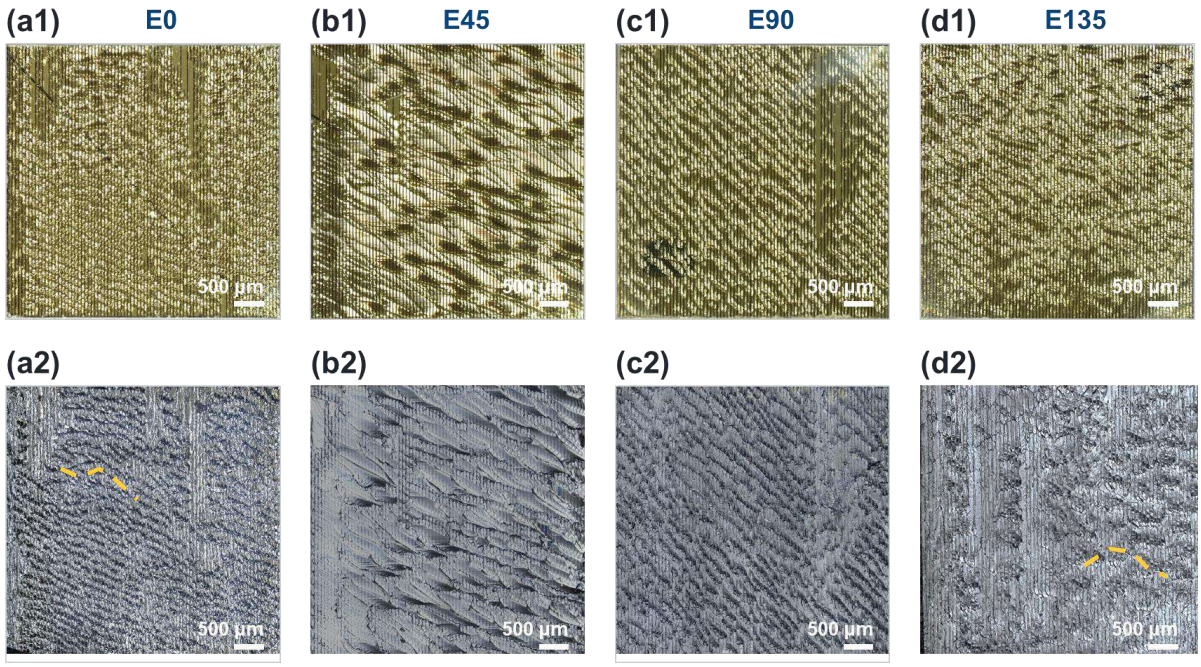


Figure 7 Effect of polarization on internal modification and separated-surface morphology at HD = 60 μm: (a) E0, (b) E45, (c) E90, and (d) E135; (a1–d1) top-view OM images before separation and (a2–d2) separated-surface images

Figure 8 presents representative surface images and the corresponding height profiles along the white dashed lines over a distance of approximately 700 μm. E0 shows frequent local

fluctuations and a pronounced valley. E45 contains a longer, continuously inclined segment, while E90 shows an extended rising segment with local height drops. E135 exhibits multiple undulations and step-like transitions. These profiles illustrate how the length of inclined segments and local height changes contribute to the overall surface relief. The fitted inclinations α are approximately 3.9°, 4.1°, 4.3°, and 3.4° for E0, E45, E90, and E135, respectively. The fitted inclinations of 3.4°–4.3° are close to the nominal off-axis angle and are consistent with the inclined and stepped morphologies reported previously [4, 10, 14].

Figure 9 compares representative confocal height maps using the same spatial scale and a common height range of −16 to 16 μm. E0 shows distributed undulations with alternating valleys and raised regions. Larger inclined regions and elongated valleys are observed for E45. E90 contains obliquely aligned high and low regions together with local deep valleys, whereas E135 shows irregular raised regions and narrow depressions.

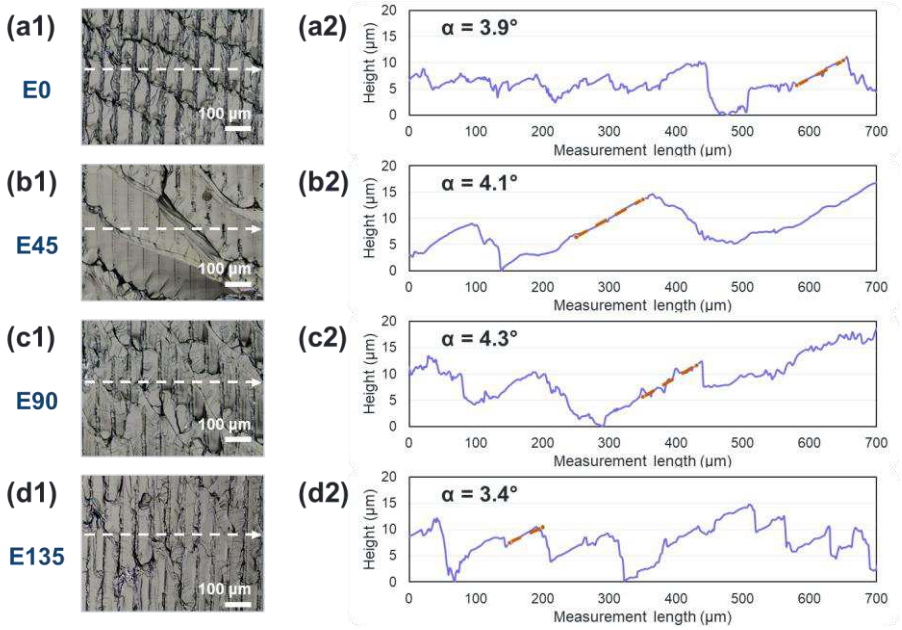


Figure 8 Separated-surface images and height profiles at HD = 60 μm: (a) E0, (b) E45, (c) E90, and (d) E135; (a1–d1) surface images with sampling paths marked by white dashed lines and (a2–d2) corresponding line profiles with fitted local inclinations α

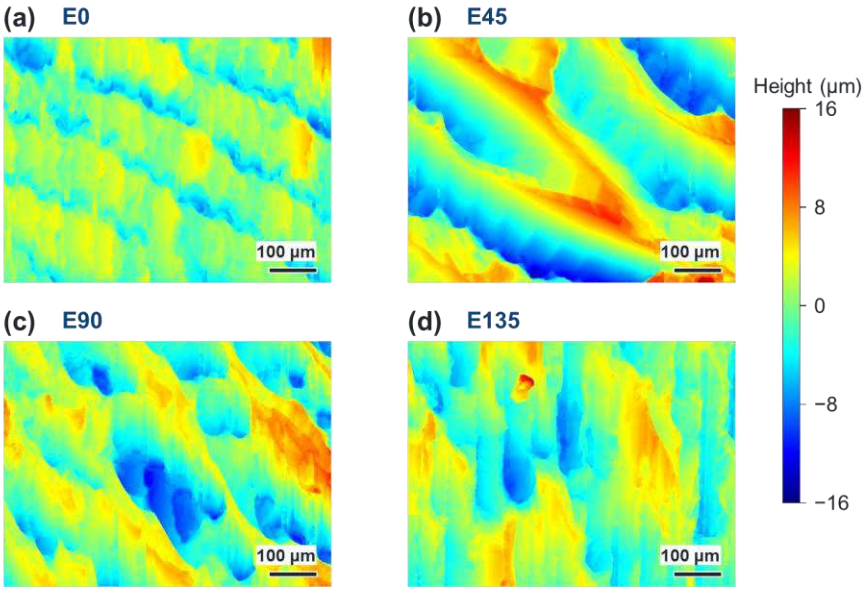


Figure 9 Confocal height maps of separated surfaces at HD = 60 µm: (a) E0, (b) E45, (c) E90, and (d) E135; all maps use a common height scale of −16 to 16 µm

Figure 10(a) compares the maximum surface height S_z for the four polarization conditions. The mean values are 15.5, 17.2, 18.9, and 17.1 µm for E0, E45, E90, and E135, respectively. E0 gives the lowest mean S_z, whereas E90 gives the highest. The aligned texture of E90 still contains local height differences, showing that a more regular directional pattern does not necessarily yield a smaller height range. The long-inclined regions and valleys of E45 also coincide with appreciable height variation.

Figure 10(b) shows mean nominal separation stresses of 20.0, 13.2, 13.4, and 20.5 MPa for E0, E45, E90, and E135, respectively. Compared with E0, the mean stresses for E45 and E90 decrease by approximately 34% and 33%, while the corresponding mean S_z values increase by approximately 11% and 22%. E45 and E90 give similar mean separation stresses, but E45 has a lower mean S_z. Conversely, E45 and E135 show similar mean S_z values with different mean separation stresses.

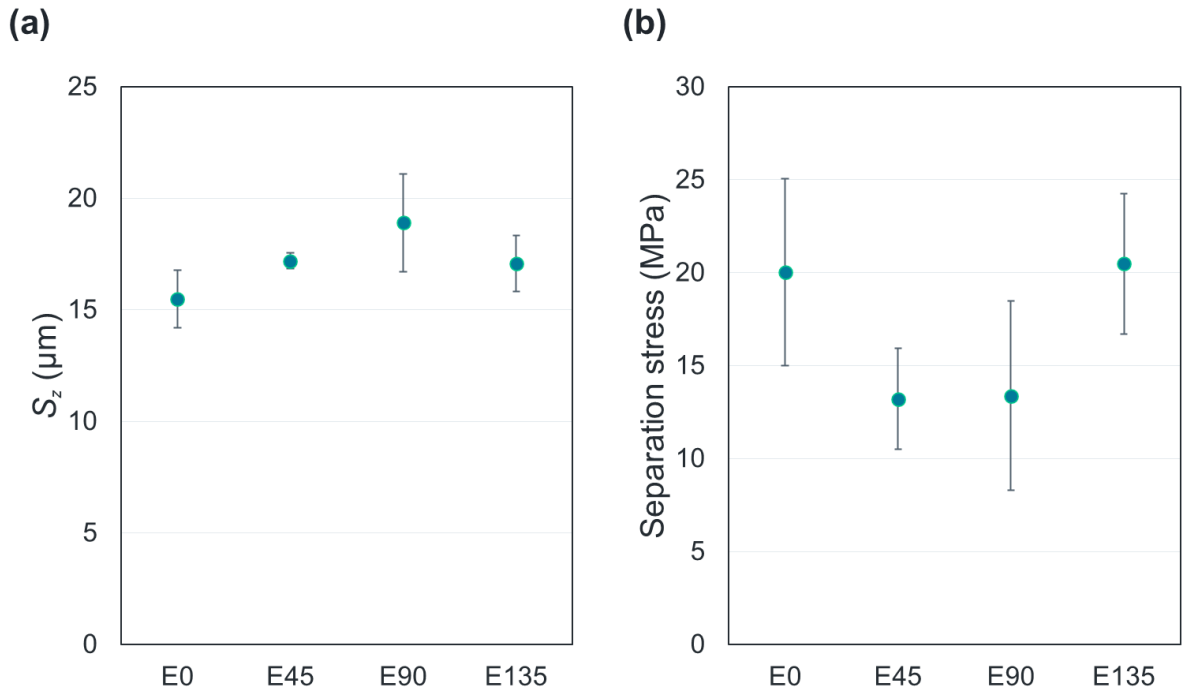


Figure 10 Effect of polarization on (a) maximum separated-surface height S_z and (b) nominal separation stress at HD = 60 μm; data points and error bars represent the mean and sample standard deviation, respectively, for three measurements in (a) and three specimens in (b)

Comparing Figure 5 and Figure 10, E0 has a greater mean local crack length but a higher mean separation stress than E45 and E90. E90 has shorter local cracks, yet its mean separation stress is close to that of E45. Previous studies have shown that the relative extent of cracked and modified regions, intersections between cracks at different depths, and residual connections can affect the load required for separation [7, 8, 10, 13]. In the present study, E45 and E90 show extended crack paths, whereas E0 and E135 mainly show local junctions. These morphologies suggest differences in the residual connections across the processed plane.

4. Conclusion

The effects of linear polarization on internal modification and slicing of n-type 4H-SiC were investigated using a dual-pulse MHz burst-mode femtosecond laser. With the incident face

and scanning geometry fixed, varying the polarization angle changed the local lateral cracks, multi-line crack morphology, and separated-surface textures. E0 yielded the lowest mean maximum surface height (S_z = 15.5 μm). E45 gave a mean separation stress close to that of E90 but a lower mean S_z of 17.2 μm, compared with 18.9 μm for E90.

Crack-path continuity and residual ligament geometry may contribute to the differences in slicing behavior. Within the investigated conditions, polarization provides a practical processing parameter for adjusting the balance between separated-surface height variation and the load required for slicing.

Author contributions

All the authors have contributed equally to the production of the present paper.

Funding

This work was supported by the National Science and Technology Council of the Republic of China under Contract NSTC 114-2221-E-A49-069 and GlobalWafers Co., Ltd.

Data availability

The data sets generated during the current study are available from the corresponding author on reasonable request.

Declarations

Conflict of interest The authors declare that they have no known competing financial interests or personal relationships that could have appeared to influence the work reported in this paper.

References

[1] P. Wang, W. Zhong, M. Wang, H. Zhao, W. Wu, P. Yan, W. Zeng, X. Jiang, Mechanisms and advances in field assisted machining of SiC, The International Journal of Advanced Manufacturing Technology 143(9) (2026) 4691–4711.

[2] Y. Yang, G. Li, T. Zhou, M. Yi, S. Qu, C. Xu, Study of surface quality during picosecond laser ablation–assisted grinding of C-face and Si-face of 4H-SiC crystals, The International Journal of Advanced Manufacturing Technology 140(1) (2025) 229–242.

[3] Y. Yamada, T. Ikeda, S. Komatsuzaki, J. Ikeno, Precision laser slicing technology for single crystal SiC wafers 2nd Report : Relationship between laser scanning direction and cleavage, Journal of the Japan Society for Abrasive Technology (2021) 549.

[4] H. Li, H. Wang, W. Cen, X. Lu, Y. Li, L. Li, Y. Yan, K. Pan, W. Guo, Crystal anisotropy-modulated laser modification for high-efficiency and low-loss exfoliation of 4H-SiC ingots, Materials & Design (2026) 116203.

[5] Y. Yao, Q. Chen, B. Li, J. Zhang, R. Wang, M. Bai, R. Liang, L. Ma, T. Ma, J. Zhang, Influence of crystal orientation and incident plane on n-type 4H-SiC wafer slicing by using picosecond laser, Optics & Laser Technology 182 (2025) 112174.

[6] Z. Qing, H. Wei, X. Chen, Y. Zhang, Regulating random crack propagation in laser slicing of 4H-SiC wafer via classification characterization and energy-crack morphology mapping, Optics & Laser Technology 203 (2026) 115515.

[7] H. Wang, Q. Cao, T. Wu, L. Yu, Z. Wang, S. Peng, D. Wang, Crack propagation mechanisms in laser slicing of 4° off-axis 4H-SiC and separation strength regulation via multi-beam processing, Materials Science in Semiconductor Processing 201 (2026) 110100.

[8] H. Wang, Q. Cao, T. Wu, Z. Wang, Y. Hou, S. Peng, D. Wang, Experimental investigation on crack evolution and separation strength in 4H-SiC slicing by sub-nanosecond laser, Optics & Laser Technology 187 (2025) 112826.

[9] Y. Yan, L. Jiang, Z. Wang, W. Zhu, X. Qi, A. Wang, D. Grojo, X. Li, High-precision laser slicing of silicon carbide using temporally shaped ultrafast pulses, Light: Advanced Manufacturing 6 (2025) 1.

[10] Y.-W. Chen, J.-F. Kuo, Y.-C. Wang, C.-W. Cheng, MHz burst-mode femtosecond laser slicing of n-type 4H-SiC wafer: From initiating to propagating cracks, CIRP Journal of Manufacturing Science and Technology 65 (2026) 336–344.

[11] M. Sun, S. Zhao, J. Du, S. Han, L. Jiang, X. Lin, X. Wang, Polarization dependences of the laser in 4H-SiC wafer slicing, Optics Express 33(10) (2025) 20682–20698.

[12] B. Li, H. Yan, Y. Lian, Y. Long, W. Ling, B. Zhang, W. Zhou, Interface weakening mechanism for Femtosecond laser slicing of semi-insulating 4H-SiC wafers, Journal of Materials Processing Technology (2026) 119482.

[13] Y.-C. Wang, J.-F. Kuo, Y.-W. Chen, C.-W. Cheng, Femtosecond-laser wafer slicing of n-type 4 H-SiC in double-pulse MHz burst mode, Applied Physics A 132(2) (2026) 93.

[14] B. Li, J. Zhang, Q. Chen, L. Che, X. Zhang, H. Fan, Y. Yao, X. Xu, X. Chen, R. Wang, Microstructural interface analysis and multilayer damage mechanism in laser-sliced 4H-SiC wafers, International Journal of Precision Engineering and Manufacturing 27(7) (2026) 2655–2678.